IOP Publishing

Smart Materials and Structures

Smart Mater. Struct. 29 (2020) 105006 (11pp)

https://doi.org/10.1088/1361-665X/ab9add

Nonlinear piezoelectric plate framework for aeroelastic energy harvesting and actuation applications

Jose Augusto de Carvalho Dias[1], **Vagner Candido de Sousa**[2], **Alper Erturk**[3] and **Carlos De Marqui Junior**[1]

[1] Department of Aeronautical Engineering, Sao Carlos School of Engineering, University of São Paulo, São Carlos, SP, 13566-590, Brazil

[2] Universidade Estadual Paulista (Unesp), Câmpus Experimental de São João da Boa Vista, São João da Boa Vista, SP, 13876-750, Brazil

[3] G. W. Woodruff School of Mechanical Engineering, Georgia Institute of Technology, Atlanta, Georgia 30332, United States of America

E-mail: demarqui@sc.usp.br

Received 17 January 2020, revised 27 May 2020
Accepted for publication 9 June 2020
Published 24 August 2020

Abstract

The use of piezoelectric materials in various applications, including the development of bio-inspired structures, vibration control, energy harvesting, among others, has been investigated by several researchers over the last few decades. In most cases, linear piezoelectricity is assumed in modeling and analysis of such systems. However, the recent literature shows that non-linear manifestations of piezoelectric materials are relevant and can modify the electromechanical behavior especially around the resonance. This work extends the investigation of non-linear piezoelectricity, by adding geometric nonlinearities and aerodynamic effects, to aeroelastic problems such as wind energy harvesting. A piezoaeroelastic model that combines a non-linear coupled finite element model and the doublet lattice model of unsteady aerodynamics is presented. The electromechanically coupled finite element model includes the non-linear behavior of piezoelectric material under weak electric fields. Model predictions are validated by experimental data for 1) a double bimorph actuation case and 2) a vibration based energy harvesting case. Later, the piezoaeroelastic behavior of a generator plate-like wing for wind energy harvesting is numerically investigated when linear as well as non-linear piezoelectricity is considered. The experimentally validated geometrically and materially non-linear framework presented here is applicable to both energy harvesting and actuation problems in the presence of air flow.

Keywords: wind energy harvesting, aeroelasticity, non-linear piezoelectricity

1. Introduction

The literature of energy harvesting exhibits a great number of papers reporting geometrically scalable and simple wind energy harvesters. The motivation is to power low consumption electronic components employed in engineering applications located in high wind areas by converting wind energy into usable electrical energy. While wind turbines are explored for large scale cases, the conversion of persistent flow induced oscillations of airfoils (Erturk *et al* 2010, De Sousa and De Marqui Junior 2015, Dias *et al* 2013, Bae and Inman 2014a, Abdelkefi *et al* 2012a, Abdelkefi *et al* 2012c), elastic wings (De Marqui *et al* 2010, De Marqui *et al* 2011, Xiang *et al* 2015, Bruni *et al* 2017) or beams in axial flow (Tang *et al* 2009, Dunnmon *et al* 2011, Michelin and Doare 2013, De Marqui *et al* 2018) by using piezoelectric materials as transduction mechanism are among the piezoelectrically linear aeroelastic energy harvester concepts and configurations available in the literature.

The typical linear flutter behavior is well known from the classical literature of aeroelasticity (Theodorsen 1935, Bisplinghoff *et al* 1996). Linear aeroelastic systems present persistent oscillations only at the linear flutter speed. Therefore, the operation envelope of linear aeroelastic based wind energy harvesters is reduced to a single airflow speed, limiting practical applications. Nonlinear aeroelastic systems, on the other hand, can offer persistent oscillations over ranges of airflow speeds due to the presence of concentrated or distributed structural nonlinearities as well as aerodynamic nonlinearities (Dowell and Tang 2002). Since real world applications often involve nonlinearities and in order to overcome the limitations of linear aeroelastic energy harvesters, there has been growing research interest in non-linear aeroelastic energy harvesters over the past few years (Abdelkefi *et al* 2012a, De Marqui *et al* 2018, Sousa *et al* 2011, Abdelkefi and Hajj 2013, Bae and Inman 2014b, De Sousa and De Marqui Junior 2015, Javed *et al* 2015).

The linear and non-linear piezoaeroelastic wind energy harvesters discussed in the literature to date have considered the use of monolithic piezoelectric materials and the 31-mode of piezoelectricity, or piezoelectric fiber composites, such as Macro-Fiber Composites (MFCs) mostly using the 33-mode of piezoelectricity. In all cases, linear piezoelectric constitutive equations (*IEEE Standard on Piezoelectricity* 1988) are taken into account during the derivation of the governing equations of linear as well as non-linear wind energy harvesters. However, nonlinearities of piezoelectric materials have been observed in sensing and/or actuation cases as well as in energy harvesting applications, modifying significantly the dynamics of electroelastic structures (compared to the linear counterparts).

Most of the non-linear modeling of piezoelectric materials has considered stiff and brittle monolithic piezoelectric materials, such as the geometrically linear and materially non-linear framework presented by Leadenham and Erturk (2015) for energy harvesting, sensing and actuation. In previous studies dealing with electroelastic structures (Aurelle *et al* 1996, Abdelkefi *et al* 2012b, Wolf and Gottlieb 2001, von Wagner and Hagedorn 2002, Mahmoodi *et al* 2008, Hu *et al* 2006, Goldschmidtboeing *et al* 2011), piezoelectric nonlinearities were explored for separate problems of actuation or sensing and similar patterns of piezoelectric softening were related to different sources (e.g. non-linear elasticity and non-linear coupling simultaneously or separately). A detailed literature review on piezoelectric nonlinearities can be found in Leadenham and Erturk (2015). Recently, an experimentally validated geometrically and materially non-linear framework for mechanical excitation of an MFC bimorph for non-linear energy harvesting (Tan *et al* 2018b) and actuation purposes (Tan *et al* 2018a) was presented, extending the linear homogenized model of Shahab and Erturk (2017).

In this paper, the effects of a piezoelectric nonlinearities on the behavior of a generator wing are investigated. The piezoaeroelastic model is obtained by combining a subsonic unsteady aerodynamic model based on the doublet-lattice method (DLM) (Albano and Rodden 1969) with an electromechanically coupled non-linear finite element (FE) model that employs von Kármán plate theory. The FE model also includes the non-linear behavior of piezoelectric MFCs which is based on a modified expression for the non-linear enthalpy. The resulting non-linear FE model is validated against experimental data for a bimorph MFC energy harvester under base excitation and also against experimental data considering MFCs as actuator. Finally, the piezoaeroelastic behavior of a non-linear generator wing is numerically investigated for a set of load resistances when the linear and non-linear MFC models are considered.

2. Theoretical model

This section presents the formulation of electromechanically coupled systems considering non-linear piezoelectricity. First, the modeling of a linear electromechanically coupled plate is briefly discussed. The modeling of non-linear piezoelectric effects is then presented and combined to linear electroelastic governing equations. Later, the von Kármán plate theory is considered to model the structure that is also combined to the non-linear piezoelectric model presented in this work. At the end of this section, the linear unsteady aerodynamic model, that is combined with the non-linear structural model to obtain a piezoaeroelastic model, is briefly presented.

2.1. Electromechanically coupled plate formulation

The equations of motion of the coupled system can be obtained from Hamilton's principle, which in the absence of electromagnetic field is defined as,

$$\delta \int_{t_0}^{t_1} \left(\int_V L dV \right) dt + \int_{t_0}^{t_1} \delta W dt = 0 \tag{1}$$

where L is the Lagrangian defined in terms of the kinetic energy (T_{ke}) and electrical enthalpy density (H) as $L = (T_{ke} - H)$, and δW is the virtual work due to external mechanical and electrical forces that will be later defined. The kinetic energy is

$$T_{ke} = \frac{1}{2} \rho \dot{\mathbf{u}}^{\mathrm{T}} \dot{\mathbf{u}} \tag{2}$$

where ρ is the mass density, $\dot{\mathbf{u}}$ is the generalized displacement field, and an overdot represents time derivative. The superscript T stands for transpose. Assuming linear piezoelectricity (linear-electroelastic constitutive relation for the piezoceramic material) (*IEEE Standard on Piezoelectricity* 1988), the enthalpy density is defined as,

$$H_{lin} = \frac{1}{2} \mathbf{S}^{\mathrm{T}} \mathbf{C}_p^{\mathrm{E}} \mathbf{S} - \mathbf{E}^{\mathrm{T}} \mathbf{e} \mathbf{S} - \frac{1}{2} \mathbf{E}^{\mathrm{T}} \varepsilon^{\mathrm{S}} \mathbf{E} \tag{3}$$

where $\mathbf{S}$ is the strain vector, $\mathbf{C}_p$ is the matrix of piezoelectric elastic stiffness constants, $\mathbf{e}$ is the matrix of piezoelectric constants, ε is the matrix of electric permittivity constants, $\mathbf{E}$ is the electric field vector, while the superscripts E and S denote that the parameters are measured at constant electric field and constant strain, respectively. The variation of mechanically applied work due to a set of discrete mechanical forces $\mathbf{f}$ and the variation of electrically extracted work for a set of discrete electric charge outputs q are combined as:

$$\delta W = \int_{V_s} \delta \mathbf{u}^{\mathrm{T}} \mathbf{f} \mathrm{d}V_s + \int_{V_p} \delta \phi^{\mathrm{T}} q \mathrm{d}V_p \tag{4}$$

where ϕ is the vector of electrical potential, V is the volume of the element, subscripts s and p stand for the substructure and piezoceramic layers.

Using equations (2), (3) and (4), the generalized Hamilton's principle for a linear electromechanically coupled structure becomes

$$\begin{aligned}\int_{t_0}^{t_1} \Big[&-\int_{V_s} \delta \mathbf{S}^{\mathrm{T}} \mathbf{C}_s \mathbf{S} \mathrm{d}V_s - \int_{V_p} \delta \mathbf{S}^{\mathrm{T}} \left(\mathbf{C}_p^{\mathrm{E}} \mathbf{S} - \mathbf{e}^{\mathrm{T}} \mathbf{E} \right) \mathrm{d}V_p \\ &+ \int_{V_p} \delta \mathbf{E}^{\mathrm{T}} \left(\mathbf{e}\mathbf{S} + \varepsilon^{\mathrm{S}} \mathbf{E} \right) \mathrm{d}V_p + \int_{V_s} \tfrac{1}{2} \rho_s \delta \mathbf{u}^{\mathrm{T}} \dot{\mathbf{u}} \mathrm{d}V_s \\ &+ \int_{V_p} \tfrac{1}{2} \rho_p \delta \mathbf{u}^{\mathrm{T}} \dot{\mathbf{u}} \mathrm{d}V_p + \delta W + \delta W_D \Big] dt = 0\end{aligned} \tag{5}$$

where $\mathbf{C}_s$ is the matrix of substructure elastic stiffness constants. δW_D denotes the work done by damping forces,

$$\delta W_D = \int_V \delta \mathbf{u}^{\mathrm{T}} \mathbf{D}_d \dot{\mathbf{u}} \mathrm{d}V \tag{6}$$

Various finite element formulations could be assumed to obtain the equations of motion for electromechanically coupled systems from equation (5). De Marqui *et al* (2009) presented the derivation of the equations of motion based on the Kirchhoff plate theory as,

$$\mathbf{M}\ddot{\mathbf{u}} + \mathbf{D}\dot{\mathbf{u}} + \mathbf{K}\mathbf{u} - \mathbf{\Theta}\mathbf{v}_p = \mathbf{f} \tag{7}$$

$$\mathbf{\Theta}^{\mathrm{T}} \dot{\mathbf{u}} + \mathbf{C}_{cap} \dot{\mathbf{v}}_p + \frac{1}{R_l} \mathbf{v}_p = 0 \tag{8}$$

where $\mathbf{M}$ is the global mass matrix, $\mathbf{K}$ is the global linear stiffness matrix, $\mathbf{\Theta}$ is the effective electromechanical coupling matrix, $\mathbf{C}_{cap}$ is the effective capacitance matrix of the MFCs, $\mathbf{D}$ is the global damping matrix (assumed as proportional to the mass and stiffness matrices), $\mathbf{v}_p$ is the resultant voltage output across a load resistance (R_l) connected to the electrodes of the piezoelectric material (MFC in the case of this work). The right-hand-side term $\mathbf{f}$ in equation (7) represents the excitation due to base motion or the vector of aerodynamic loads in a piezoaeroelastic case. Details on the formulation and expression of each matrix can be found in De Marqui *et al* (2009).

In this work, however, the goal is to model the non-linear piezoelectric behavior of MFCs. Therefore, we implement the following expression for the non-linear enthalpy,

$$\begin{aligned}H_{nonl} = \tfrac{1}{2} \mathbf{S}^{\mathrm{T}} \mathbf{C}_p^{\mathrm{E}} \mathbf{S} + \mathbf{S}^{\mathrm{T}} \mathbf{C}_1^{\mathrm{E}} \alpha \left\{ \mathbf{I} - \mathrm{diag} \left[\exp \left(|\mathbf{S}|^{\beta} \tau \right) \right] \right\} \mathbf{S} \\ - \mathbf{E}^{\mathrm{T}} \mathbf{e} \mathbf{S} - \tfrac{1}{2} \mathbf{E}^{\mathrm{T}} \gamma_{11} \mathbf{S} |\mathbf{S}| - \tfrac{1}{2} \mathbf{E}^{\mathrm{T}} \varepsilon^{\mathrm{S}} \mathbf{E}\end{aligned} \tag{9}$$

where $\mathbf{C}_1^{\mathrm{E}}$ is the non-linear piezoelectric elasticity matrix at a constant electric field, γ_{11} is the non-linear quadratic coupling matrix, α is a consent that quantifies the percentage of softening of the MFC stiffness, β is a coefficient that regulates the piezoelectric softening with increasing strain, and τ is a negative coefficient that regulates the maximum softening and strain relation.

Several models based on deformation and electric field (when applied to symmetrical structures, as in the bimorph case) result in the cancelation of second order terms as discussed in Leadenham and Erturk (2015). In this work we propose the modeling of the electric enthalpy density based on the deformation modulus. Through the compatibility relations ($\mathbf{T}_{ij} = \partial H / \partial \mathbf{S}_{ij}$ and $\mathbf{D}^e = -\partial H / \partial \mathbf{E}$), the stress vector $\mathbf{T}$ is defined as

$$\begin{aligned}\mathbf{T} = \mathbf{C}_p^{\mathrm{E}} \mathbf{S} - \mathbf{e}^{\mathrm{T}} \mathbf{E} - \mathrm{diag} \left(|\mathbf{S}| \right) {\gamma_{11}}^{\mathrm{T}} \mathbf{E} \\ + 2 \mathbf{C}_1^{\mathrm{E}} \alpha \Big\{ \mathbf{I} - \mathrm{diag} \left[\exp \left(|\mathbf{S}|^{\beta} \tau \right) \right] \\ \times \left[\mathbf{I} - \mathrm{diag} \left(\frac{1}{2} \beta \tau \mathbf{S}^2 |\mathbf{S}|^{\beta - 2} \right) \right] \Big\} \mathbf{S}\end{aligned} \tag{10}$$

and the electric displacement $\mathbf{D}^e$ is defined as

$$\mathbf{D}^e = \mathbf{e} \mathbf{S} + \frac{1}{2} \gamma_{11} \mathrm{diag} \left(|\mathbf{S}| \right) \mathbf{S} + \varepsilon^{\mathrm{S}} \mathbf{E} \tag{11}$$

Considering the non-linear piezoelectric elasticity matrix, as an approximation, equal to the half of the linear stiffness matrix, equation (10) simplifies to

$$\begin{aligned}\mathbf{T} = \mathbf{C}_p^{\mathrm{E}} \mathbf{S} - \mathbf{e}^{\mathrm{T}} \mathbf{E} + \mathbf{C}_p^{\mathrm{E}} \alpha \left\{ \mathbf{I} - \mathrm{diag} \left[\exp \left(|\mathbf{S}|^{\beta} \tau \right) \right] \right\} \mathbf{S} \\ - \mathrm{diag} \left(|\mathbf{S}| \right) {\gamma_{11}}^{\mathrm{T}} \mathbf{E}\end{aligned} \tag{12}$$

when high order strain terms are neglected.

The generalized Hamilton's principle (equation (1)) for the non-linear case can be written as

$$\begin{aligned}\int_{t_0}^{t_1} \Big[&-\int_{V_p} \delta \mathbf{S}^{\mathrm{T}} \Big(\mathbf{C}_p^{\mathrm{E}} \mathbf{S} + \mathbf{C}_p^{\mathrm{E}} \alpha \left\{ \mathbf{I} - \mathrm{diag} \left[\exp \left(|\mathbf{S}|^{\beta} \tau \right) \right] \right\} \mathbf{S} \\ &- \mathbf{S} \mathrm{diag} \left(|\mathbf{S}| \right) {\gamma_{11}}^{\mathrm{T}} \mathbf{E} - \mathbf{e}^{\mathrm{T}} \mathbf{E} \Big) \mathrm{d}V_p - \int_{V_s} \delta \mathbf{S}^{\mathrm{T}} \mathbf{C}_s \mathbf{S} \mathrm{d}V_s \\ &- \int_{V_p} \delta \mathbf{E}^{\mathrm{T}} \left(-\mathbf{e}\mathbf{S} - \tfrac{1}{2} \gamma_{11} \mathrm{diag} \left(|\mathbf{S}| \right) \mathbf{S} - \varepsilon^{\mathrm{S}} \mathbf{E} \right) \mathrm{d}V_p \\ &+ \int_{V_s} \tfrac{1}{2} \rho_s \delta \mathbf{u}^{\mathrm{T}} \dot{\mathbf{u}} \mathrm{d}V_s + \int_{V_p} \tfrac{1}{2} \rho_p \delta \mathbf{u}^{\mathrm{T}} \dot{\mathbf{u}} \mathrm{d}V_p + \delta W + \delta W_D \Big] dt = 0\end{aligned} \tag{13}$$

and by considering, for example, linear plate finite element model (De Marqui *et al* 2009) as well as equations (11) and (12), the global equations of motion for a linear plate combined to a non-linear piezoelectric model are given by

$$\mathbf{M}\ddot{\mathbf{u}} - \mathbf{D}\dot{\mathbf{u}} + \mathbf{K}(\mathbf{u}) \mathbf{u} - \mathbf{\Theta}\mathbf{v}_p = \mathbf{f} \tag{14}$$

$$\mathbf{\Theta}^{\mathrm{T}} \dot{\mathbf{u}} + \mathbf{C}_{cap} \dot{\mathbf{v}}_p + \frac{1}{R_l} \mathbf{v}_p = 0 \tag{15}$$

where $\mathbf{K}(\mathbf{u})$ and $\mathbf{\Theta}$ are redefined as non-linear matrices,

$$\begin{aligned}\mathbf{K}_i (\mathbf{u}) = \int_{V_s} z^2 {\mathbf{B}_K}^{\mathrm{T}} \mathbf{C}_s \mathbf{B}_K \mathrm{d}V_s \\ + \int_{V_p} z^2 {\mathbf{B}_K}^{\mathrm{T}} \mathbf{C}_p^{\mathrm{E}} \left(\mathbf{I} + \alpha \left\{ \mathbf{I} - \mathrm{diag} \left[\exp \left(|\mathbf{S}|^{\beta} \tau \right) \right] \right\} \right) \mathbf{B}_K \mathrm{d}V_p\end{aligned} \tag{16}$$

$$\boldsymbol{\Theta}_i = -\int_{V_p} \left[z\mathbf{B}_K{}^{\mathrm{T}} \left(\mathbf{e}^{\mathrm{T}} + \mathrm{diag}\left(|\mathbf{S}|\right)\gamma_{11}{}^{\mathrm{T}}\right)\mathbf{B}_E\right] \mathrm{d}V_p \tag{17}$$

where

$$\mathbf{B}_K = \left\{ \begin{array}{ccc} \frac{\partial^2 \boldsymbol{\Gamma}}{\partial x^2} & \frac{\partial^2 \boldsymbol{\Gamma}}{\partial y^2} & 2\frac{\partial^2 \boldsymbol{\Gamma}}{\partial x \partial y} \end{array} \right\}^{\mathrm{T}}, \tag{18}$$

$\boldsymbol{\Gamma}$ is the element shape function vector and $\mathbf{B}_E = \left\{ \begin{array}{ccc} 0 & 0 & z/b_{mfc} \end{array} \right\}^{\mathrm{T}}$. Note that the expressions for non-linear stiffness and non-linear electromechanical coupling (equations (16) and (17)) depend on the solution of the problem itself. That is, the terms containing the non-linear stiffness and the non-linear coupling are dependent on the deformation, which will be found only after solving the coupled equations.

2.2. Nonlinear geometric formulation

Geometric non-linearity is present due to large displacements of the proposed flexible structure. The von Kármán plate theory, which is valid for moderate displacements, is considered in the model formulation to properly represent structural behavior. When the displacements are moderately large, then an interaction between the membrane and bending effects is initiated due to transverse displacements. Von Karman (1910) first studied this effect. In his theory, this effect is incorporated using a simplified form of the Green-Lagrange deformations obtained when the non-linear terms associated with the components of the displacement in the directions of the plate plane, u_x and u_y, are neglected (Crisfield 1997). Thus the deformation becomes,

$$\mathbf{S}_{green} = \left\{ \begin{array}{c} S_{xx} \\ S_{yy} \\ 2S_{xy} \end{array} \right\} = \left\{ \begin{array}{c} u_{,x} + w_{,x}{}^2/2 \\ v_{,y} + w_{,y}{}^2/2 \\ u_{,y} + v_{,x} + w_{,x}w_{,y} \end{array} \right\} - z\left\{ \begin{array}{c} w_{,x^2} \\ w_{,y^2} \\ 2w_{,xy} \end{array} \right\} = \mathbf{S}^p - z\mathbf{K}^b \tag{19}$$

where $\mathbf{S}^p$ denote the in plane deformations and $\mathbf{K}^b$ denote the curvature changes due to bending. The derivatives with respect to a variable are denoted in the subscript after the comma ($\partial * / \partial x = *_{,x}$). Nonlinear terms with second and higher order derivatives are neglected in this equation.

The finite element approach for the geometrically non-linear problem is based on Zienkiewicz and Taylor (2000) in combination with equation (19). The variational $\mathbf{S}^p$ and $\mathbf{K}^b$ can be written respectively as

$$\delta\mathbf{S}^p = \mathbf{B}^\alpha \delta\mathbf{u}_\alpha = \left[\begin{array}{cc} \Gamma_{\alpha,x} & 0 \\ 0 & \Gamma_{\alpha,y} \\ \Gamma_{\alpha,y} & \Gamma_{\alpha,x} \end{array} \right] \left\{ \begin{array}{c} \delta u_\alpha \\ \delta v_\alpha \end{array} \right\} + \left[\begin{array}{cc} w_{,x} & 0 \\ 0 & w_{,y} \\ w_{,y} & w_{,x} \end{array} \right] \mathbf{G}_\alpha \left\{ \begin{array}{c} \delta w_\alpha \\ \delta\theta_{x\alpha} \\ \delta\theta_{y\alpha} \end{array} \right\} = \mathbf{B}_P^\alpha \delta\tilde{\mathbf{u}}_\alpha + \mathbf{B}_L^\alpha \delta\tilde{\boldsymbol{w}}_\alpha \tag{20}$$

$$\delta\mathbf{K}^b = \left[\begin{array}{ccc} \Gamma^w_{\alpha,xx} & \Gamma^{\theta x}_{\alpha,xx} & \Gamma^{\theta y}_{\alpha,xx} \\ \Gamma^w_{\alpha,yy} & \Gamma^{\theta x}_{\alpha,yy} & \Gamma^{\theta y}_{\alpha,yy} \\ 2\Gamma^w_{\alpha,xy} & 2\Gamma^{\theta x}_{\alpha,xy} & 2\Gamma^{\theta y}_{\alpha,xy} \end{array} \right] \left\{ \begin{array}{c} \delta w_\alpha \\ \delta\theta_{x\alpha} \\ \delta\theta_{y\alpha} \end{array} \right\} = \mathbf{B}_K^\alpha \delta\tilde{\mathbf{w}}_\alpha \tag{21}$$

where

$$\mathbf{G}_\alpha = \left[\begin{array}{ccc} \Gamma^w_{\alpha,x} & \Gamma^{\theta x}_{\alpha,x} & \Gamma^{\theta y}_{\alpha,x} \\ \Gamma^w_{\alpha,y} & \Gamma^{\theta x}_{\alpha,y} & \Gamma^{\theta x}_{\alpha,y} \end{array} \right] \tag{22}$$

with nodal displacement parameters defined as

$$\mathbf{u}_\alpha^{\mathrm{T}} = \left[\begin{array}{cc} \left\{ \begin{array}{cc} u_\alpha & v_\alpha \end{array} \right\} & \left\{ \begin{array}{ccc} w_\alpha & \theta_{x\alpha} & \theta_{y\alpha} \end{array} \right\} \end{array} \right] = \left[\begin{array}{cc} \tilde{\boldsymbol{u}}_\alpha^{\mathrm{T}} & \tilde{\boldsymbol{w}}_\alpha^{\mathrm{T}} \end{array} \right] \tag{23}$$

Grouping the deformation matrices as

$$\bar{\mathbf{B}}_\alpha = \left[\begin{array}{cc} \mathbf{B}_P^\alpha & \mathbf{B}_L^\alpha \\ 0 & \mathbf{B}_K^\alpha \end{array} \right] \tag{24}$$

then matrix $\mathbf{K}_i(\mathbf{u})$ becomes

$$\mathbf{K}_i(\mathbf{u}) = \int_{V_s} \bar{\mathbf{B}}_\alpha^{\mathrm{T}} \left[\begin{array}{cc} \mathbf{C}_s & 0 \\ 0 & z^2\mathbf{C}_s \end{array} \right] \bar{\mathbf{B}}_\alpha \mathrm{d}V_s \tag{25}$$

2.2.1. Nonlinear resultant formulation.

The non-linear geometric stiffness matrix in this non-linear structural case is also evaluated over the area covered by piezoelectric material (MFCs in our case) similarly as developed for the substructure in section 2.2. This geometrically non-linear model can be associated with the non-linear constitutive behavior of piezoelectric material, obtained from the non-linear enthalpy (equation (9)). The resultant non-linear electroelastic stiffness element matrix is defined as

$$\mathbf{K}^i_{nl}(\mathbf{u}) = \int_{V_s} \bar{\mathbf{B}}_\alpha^{\mathrm{T}} \left[\begin{array}{cc} \mathbf{C}_s & 0 \\ 0 & z^2\mathbf{C}_s \end{array} \right] \times \bar{\mathbf{B}}_\alpha \mathrm{d}V_s + \int_{V_p} \bar{\mathbf{B}}_\alpha^{\mathrm{T}} \left[\begin{array}{cc} \mathbf{C}^* & 0 \\ 0 & z^2\mathbf{C}^* \end{array} \right] \bar{\mathbf{B}}_\alpha \mathrm{d}V_p \tag{26}$$

where $\mathbf{C}^* = \mathbf{C}_p^{\mathrm{E}}\left(\mathbf{I} + \alpha\left\{\mathbf{I} - \mathrm{diag}\left[\exp\left(|\mathbf{S}|^\beta \tau\right)\right]\right\}\right)$ and the non-linear coupling element matrix is defined as

$$\boldsymbol{\Theta}^i_{nl} = -\int_{V_p} \bar{\mathbf{B}}_\alpha^{\mathrm{T}} \left(\mathbf{e}^{\mathrm{T}} + \mathrm{diag}\left(|\mathbf{S}|\right)\gamma_{11}{}^{\mathrm{T}}\right) \bar{\mathbf{B}}_E \mathrm{d}V_p \tag{27}$$

where $\bar{\mathbf{B}}_E = \{\ 1/b_{mfc} \quad 0 \quad 0 \quad 0 \quad z/b_{mfc}\ \}^{\mathrm{T}}$. To solve the non-linear equations for the elastic or electroelastic cases, a Newton Raphson scheme is adopted. The proposed geometrically non-linear FE model was tested against non-linear Abaqus results in static condition.

2.3. The doublet lattice model

The linearized formulation for the oscillatory, inviscid, subsonic lifting surface theory relates the normal velocity at the surface of a body (*e.g.*, an elastic wing) with the aerodynamic loads caused by the pressure distribution (Albano and Rodden 1969). The formulation is derived using the unsteady Euler equations of the surrounding fluid. The doublet singularity or a sheet of doublets is a solution of the aerodynamic potential equation. The unsteady aeroelastic phenomena of interest in this paper as well as the resultant differential pressure across the surface of a wing can be represented with this solution.

The relation between the differential pressure across the surfaces and the velocity normal to the surface of a wing is given by a kernel function (Albano and Rodden 1969). The kernel function is a closed-form solution of the integro-differential equation based on the assumption of harmonic motion. The velocity field normal to the surface of a wing is given by the equation

$$\bar{w}(x,y,z) = \frac{-1}{4V_\infty \pi \rho_0} \int\int_S \Delta p(x,y,z) K(x-\xi, y-\eta, z)\, d\xi d\eta \tag{28}$$

where $\Delta p(x,y,z)$ is the differential pressure, V_∞ is the airflow speed, ρ_0 is the air density, and ξ and η are dummy variables of integration over the wing area S in the spanwise (x) and chordwise (y) directions, respectively. The transverse direction is represented as z, while K is the kernel function given as

$$K(x-\xi, y-\eta, z) = \exp\left(\frac{-j\omega(x-\xi)}{V_\infty}\right)\frac{\partial^2}{\partial z^2} \left\{\frac{1}{\bar{R}}\exp\left[\frac{j\omega}{V_\infty \chi^2}(\lambda - M\bar{R})\right] d\lambda\right\} \tag{29}$$

where $\chi^2 = 1 - M^2$ and $\bar{R} = \sqrt{(x-\xi)^2 + (y-\eta)^2 + z^2}$, ω is the excitation frequency, M is the Mach number, and λ is a dummy variable. The DLM provides an approximate solution for the kernel function. The wing is represented by a thin lifting surface divided into a number of elements (panels or boxes) associated with doublet singularities. The singularities have constant strength in the chordwise direction and parabolic strength in the spanwise direction. A line of doublets distribution of acceleration potential is assumed at the 1/4 chord line of each panel, which is equivalent to a pressure jump across the surface. A control point, where the boundary condition is verified, is defined in the half span of each element at the 3/4 chord line. The strengths of the oscillating potential placed at the 1/4 chord lines are the unknowns of the problem.

The downwash, introduced by the lifting lines, is assumed to be harmonic and is checked at each control point. Integration over the surface gives the local and the total aerodynamic force coefficients (Albano and Rodden 1969). The solution of the resulting matrix equation is

$$\mathbf{f} = \mathbf{AIC}^{-1}(\omega)\,\mathbf{w_a} \tag{30}$$

where $\mathbf{AIC}^{-1}(\omega)$ is the matrix of aerodynamic influence coefficients (related to the kernel function) at a specific frequency (ω), and $\mathbf{w_a}$ is the downwash vector,

$$\mathbf{w_a} = \frac{\partial \mathbf{W}}{\partial t} + V_\infty \frac{\partial \mathbf{W}}{\partial x} \tag{31}$$

where $(\mathbf{W})$ is the plate transverse displacement.

2.3.1. Piezoaeroelastically Coupled Equations.

The aerodynamic loading and the structural motion are obtained from distinct numerical methods with distinct meshes so that transformation matrices are determined using a surface spline scheme to interpolate the forces in the aerodynamic mesh into the nodes of the FE mesh (Harder and Desmarais 1972). Therefore, the aerodynamic forces are evaluated as

$$\mathbf{f}(\omega) = \mathbf{\Phi}^{\mathrm{T}} G_{ma} \mathbf{AIC}^{-1}\left(\frac{\partial}{\partial t} + V_\infty \frac{\partial}{\partial x}\right) G_{am} \mathbf{\Phi} \boldsymbol{\eta} \tag{32}$$

where G_{ma} and G_{am} are the splines connecting the aerodynamic and structural meshes, $\mathbf{\Phi}$ is the modal shape matrix and $\boldsymbol{\eta}$ is the modal coordinates vector.

The aerodynamic forces in frequency domain are converted to time domain by using a minimum square approximation to obtain a rational polynomial formulation (Roger 1977). Subsequently, the piezoaeroelastic equations can be represented in state-space form as

$$\begin{Bmatrix} \dot{\mathbf{X}}_1 \\ \dot{\mathbf{X}}_2 \\ \dot{\mathbf{v}}_p \\ \dot{\mathbf{X}}_S \end{Bmatrix} = \begin{bmatrix} 0 & \mathbf{I} & 0 & 0 \\ -\bar{\mathbf{M}}_{ae}^{-1}\bar{\mathbf{K}}_{ae}(\mathbf{u}) & -\bar{\mathbf{M}}_{ae}^{-1}\bar{\mathbf{D}}_{ae} & \bar{\mathbf{M}}_{ae}^{-1}\bar{\mathbf{\Theta}} & \bar{\mathbf{M}}_{ae}^{-1}\mathbf{A} \\ 0 & \frac{-\bar{\mathbf{\Theta}}^{\mathrm{T}}}{R_l} & \frac{-1}{R_l \mathbf{C}_{cap}} & 0 \\ 0 & \mathbf{I} & 0 & \frac{V_\infty}{b}\lambda_{ae}\mathbf{I} \end{bmatrix} \times \begin{Bmatrix} \mathbf{X}_1 \\ \mathbf{X}_2 \\ \mathbf{v}_p \\ \mathbf{X}_S \end{Bmatrix} \tag{33}$$

where $\mathbf{X}_1$ is the modal amplitudes vector, $\mathbf{X}_2$ is the first time derivative of the modal amplitudes vector, $\mathbf{X}_S$ is the aerodynamic lag state vector, $\mathbf{I}$ is the identity matrix, b is the semi-chord of the wing, λ is the lag aerodynamic root, the overbar represents modal matrices and the subscript *ae* represents the aeroelastic modified matrices.

3. Results

In this section, the non-linear numerical model presented in this work (non-linear finite element model combined to the non-linear piezoelectric model) is validated for two different cases. First, the model predictions are validated against experimental results previously presented in the literature for an MFC bimorph cantilever under base excitation in a vibration based energy harvesting problem. Later, the numerically predicted behavior of a double bimorph structure under piezoelectric bending actuation is validated against experimental results. Moreover, the system behavior for pure twist actuation and bending-twist combined actuation is discussed. Having validated the non-linear model, the last case discusses the effects of non-linear piezoelectricity on the behavior of an electromechanically coupled wing for energy harvesting. The non-linear model (equations (14) and (15) combined with equations (26) and (27)) is solved using the method of harmonic balance (Nayfeh and Mook 2008) for all acceleration and voltage actuation levels considered in each validation case. Since the excitation is assumed to be harmonic, the mechanical response solution is expected to have the same period as the electrical excitation and can be approximated by truncated Fourier series expansions. Seven harmonics are considered to predict the electroelastic response in each case.

3.1. Nonlinear MFC energy harvesting validation

The electromechanical structure as well as the experimental data of Tan *et al* (2018b) are considered for the experimental validation of the non-linear model proposed here (non-linear formulation of section 2.2.1). Two MFC laminates (M8514-P1, from Smart Material Corp.) were vacuum-bonded together without any substrate to form a bimorph structure. The structure has overall dimensions of 83.5 mm (length), 10.0 mm (width) and 0.6 mm (thickness). The overhang (active) area is 75.5 mm long and 7.0 mm wide, with a measured capacitance of 3.4 nF.

In Tan *et al* (2018b) the bimorph structure was tested under different base acceleration levels, sweeping the excitation frequency up and down around the first resonant frequency. The velocity of the MFC bimorph was measured near the center line of the free end of the cantilever. Among the set of load resistances considered by the authors, 1.3 MΩ is the one that gives the maximum power output and will be considered in this work for model validation. The experimental data of Tan *et al* (2018b) is reproduced in figures 1 and 2 along with the novel numerical results of this paper. The non-linear terms that form the non-linear stiffness matrix (equation (16)) were obtained as $\alpha = 0.365$, $\beta = 1.15$ and $\tau = -1.30$. While Tan *et al* (2018b) assume the piezoelectric non-linearity as quadratic hysteretic softening combined with cubic geometric nonlinearities, recall that we consider the exponential enthalpy model of section 2.

Figure 1 displays the numerical and experimental RMS velocity around the first resonance of the bimorph. The experimental softening behavior (with increasing excitation levels) is properly predicted by the numerical model. The resonant frequency decreased from 40.5 Hz to 30.3 Hz with increasing base acceleration level due to the softening behavior of the piezoelectric material. The numerical model accurately predicted the experimental backbone curve over the range of base excitation levels considered in Tan *et al* (2018b). Moreover, the velocity amplitudes were accurately predicted for the set of base acceleration in figure 1.

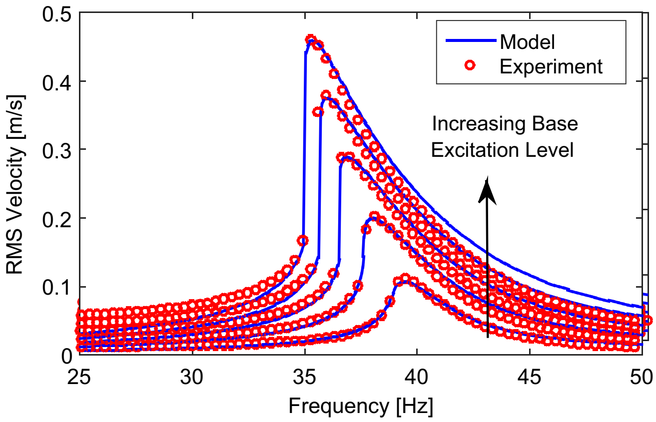

Figure 1. Experimental RMS tip velocity of the MFC bimorph versus frequency at RMS base acceleration levels of 0.1 g, 0.2 g, 0.3 g, 0.4 g, and 0.5 g using a downward frequency sweep (Tan *et al* 2018b) compared to numerical model results considering a 1.3 MΩ resistance in the electrical circuits.

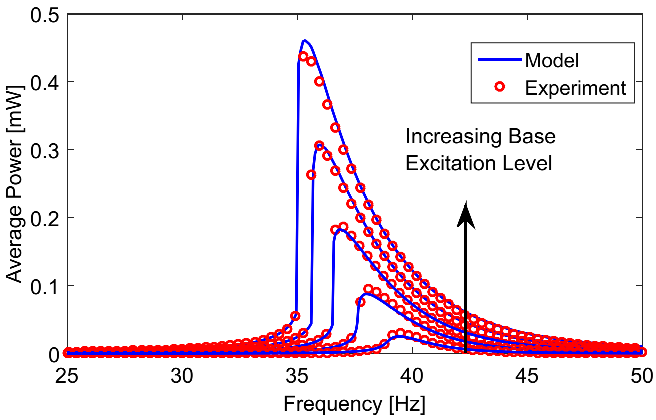

Figure 2. Experimental average power output of the MFC bimorph versus frequency at RMS base acceleration levels of 0.1 g, 0.2 g, 0.3 g, 0.4 g, and 0.5 g using a downward frequency sweep (Tan *et al* 2018b) compared to numerical model results considering a 1.3 MΩ resistance in the electrical circuits.

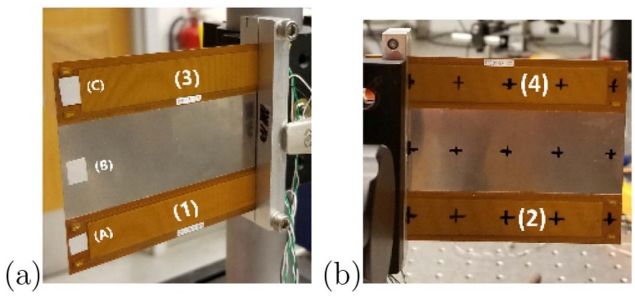

Figure 3. Double-bimorph structure with MFC laminates and stainless-steel substrate: (a) top view, with the tip velocity measurement points, and (b) bottom view, with displacement measurement points.

Table 1. Properties of an MFC representative volume element.

Property	RVE	Electrode	MFC
E_1 [Pa]	43.78×10^9	30.48×10^9	27.87×10^9
E_2 [Pa]	20.45×10^9	4.05×10^9	16.89×10^9
G_{12} [Pa]	7.35×10^9	1.49×10^9	4.94×10^9
ν_{12}	0.31	0.34	0.32
ν_{21}	0.15	0.045	0.18
ρ [Kg·m^{-3}]	6859	2964	4915

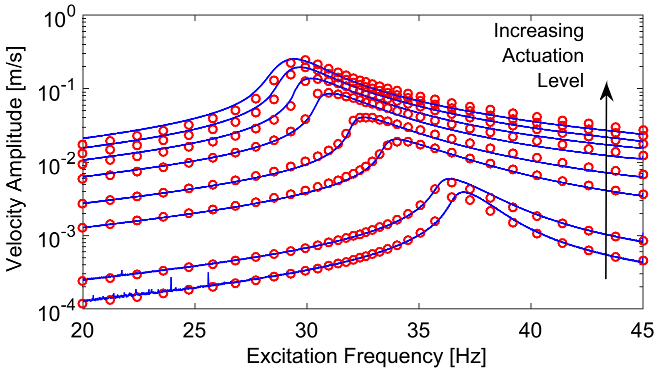

Figure 4. Experimental (contiuous lines) and numerical (markers) tip velocity of the MFC double-bimorph structure for pure bending resonant actuation with input voltages of 0.5 V, 1 V, 5 V, 10 V, 20 V, 30 V, 40 V, and 50 V.

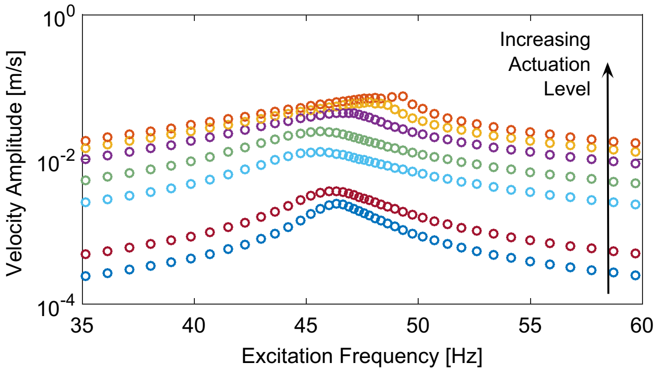

Figure 5. Numerical tip velocity of the MFC double-bimorph structure for pure twist resonant actuation with input voltages of 0.5 V, 1 V, 5 V, 10 V, 20 V, 30 V, and 40 V.

The average electrical power output (defined as $P_{avg} = v^2_{p,RMS}/R_l$) is displayed in figure 2 for different base acceleration levels. Although the model slightly overpredicts the experimental ones for high base aceleration levels, in general, good agreement is observed between numerical and experimental results. This discrepancy is likely due to dissipative terms in the electrical domain (e.g. dielectric loss) not accounted for in the present work.

3.2. Nonlinear MFC actuation validation

This section presents the experimental validation of the numerical model of section 2.2.1 (non-linear structural model and

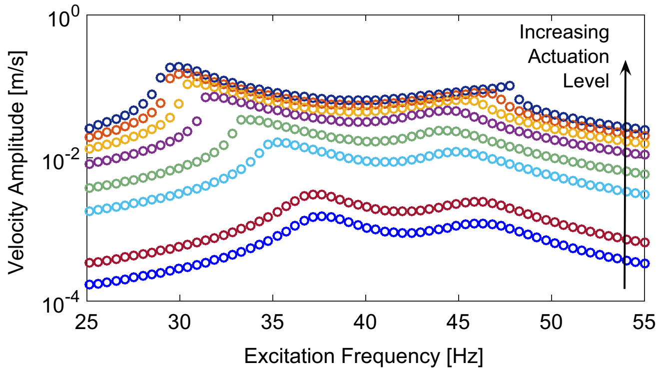

Figure 6. Numerical tip velocity of the MFC double-bimorph structure for combined bending-twist resonant actuation with input voltages of 0.5 V, 1 V, 5 V, 10 V, 20 V, 30 V, 40 V, and 50 V.

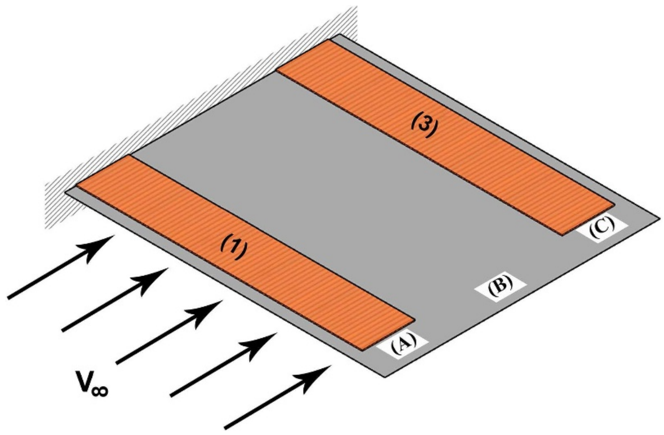

Figure 7. Schematic of the double bimorph structure under airflow excitation.

non-linear piezoeletricity) for resonant actuation of an MFC bimorph. Two MFC laminates (M8514-P1, from Smart Material Corp.) were bonded onto each side of a steel plate (Fatigue-Resistant 301 Stainless Steel Sheet), as displayed in figures 3(a) (top view) and 3(b) (bottom view). This electromechanically coupled plate is called a double-bimorph structure in this work. The steel plate has dimensions of 84.4 mm (length), 73.0 mm (width), and 0.05 mm (thickness). Each MFC has an overall size of 84.4 mm × 20.0 mm, with an active region of 76.35 mm × 14.0 mm and thickness of 0.3 mm. The plate material has an elastic modulus of 193 GPa and mass density of 7850 kg·m^{-3}. The capacitance of the active region of each MFC was measured as 4 nF.

In figure 3(a), the labels (A), (B) and (C) indicate the points of transverse velocity measurement. By considering mixing rules (Deraemaeker *et al* 2009), the properties of an MFC representative volume element were obtained, which are displayed in table 1.

The double-bimorph structure was tested in pure bending resonant actuation (with symmetric actuation on both bimorphs). Increasing voltage levels from 0.5 V up to 50.0 V were applied across the electrodes of the MFCs while sweeping the excitation frequency up and down. For the actuation

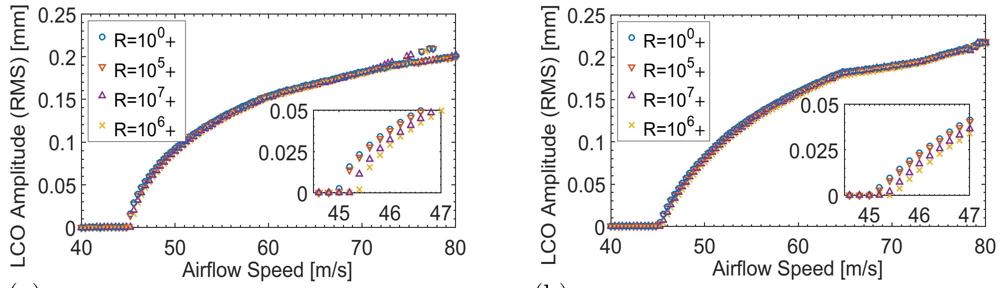

Figure 8. Numerical RMS tip displacement of the double-bimorph for increasing airflow speed and considering (a) linear and (b) non-linear MFC models for load resistances of 1 Ω, 100 kΩ, 1 MΩ, and 10 MΩ.

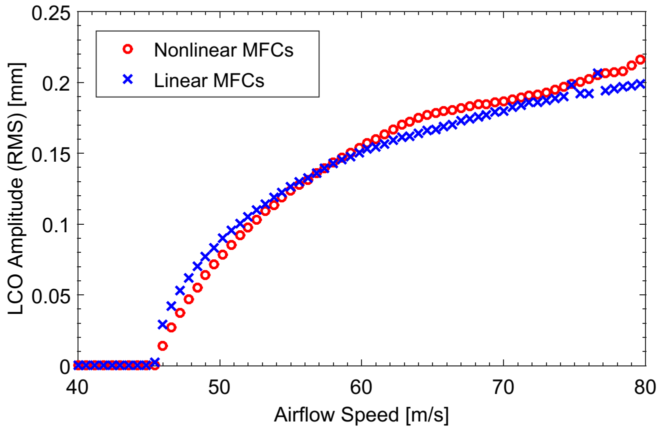

Figure 9. RMS wing tip displacement of the double-bimorph for increasing airflow speeds and considering linear and non-linear MFC models. A load resistance of 1 MΩ was assumed in the simulations.

tests, three Polytec PDV-100 portable digital vibrometers were used to measure the velocity at three measurement points (A, B and C in figure 3(a)) simultaneously (reducing differences between results due to different shapes). Data were acquired using a National Instruments NI USB-4431 board. The structure was mounted vertically to reduce the gravity effects in the results. The numerical predictions and experimental tip velocity at point A (see figure 3(a)) for pure bending resonant actuation is shown in figure 4. The numerical model properly predicts the experimental backbone curve and mechanical amplitudes for the range of voltage levels considered in figure 4. In the simulations, the constants of the non-linear stiffness matrix (equation (16)) were taken as $\alpha = 0.437$, $\beta = 0.75$ and $\tau = -7.71$.

The behavior of the MFC double bimorph is then discussed for a pure twist and also for combined bending-twist actuation cases. Although experiments were not performed for those cases, the discussion is presented according to the expected behavior described in the literature (Samur 2013). Figure 5 displays the numerical tip velocity at point A for pure twisting resonant actuation case. To create twist motion in the simulations, each bimorph pair was actuated 180° out-of-phase relative to the other pair. Softening behavior is expected until certain actuation level due to piezoelectric nonlinearities and then, for higher actuation levels, hardening should be observed due to geometric nonlinearities. Figure 5 displays the softening behavior from 0.5 V to 10 V due to the MFCs non-linear behavior while the hardening is related to the non-linear geometric behavior of the plate for higher acutation levels. The non-linear geometric behavior is more pronounced for the twist motion (compared to pure bending case) since internal stresses lead to larger stiffness than the one observed in the pure bending case of figure 4.

Figure 6 shows the tip velocity of the MFC doubel-bimorph structure for resonant bending-twist actuation. The combined actuation is obtained by applying a signal with 90° of phase between the bimorphs. Softening and hardening nonlinearities should be observed for the bending and twist modes (Samur 2013), respectively, as also displayed in figure 6. Piezoelectric softening is more pronounced in the first bending mode, while the resonant frequency of the twist mode increases for higher actuation levels due to geometric hardening. Therefore, the predicted non-linear behavior for pure twist and combined actuation cases is in agreement with the literature.

3.3. Wind energy harvesting results

In the numerical studies of this subsection, the MFC double bimorph plate presented in subsection 3.2 is considered in a wind energy harvesting case. The aeroelastic behavior of the electroelastic structure is investigated for a range of airflow speeds by combining the structural model of section 2.2.1 with the DLM presented in section 2.3. As a reference case, when the linear structural model is considered (equations (7) and (8) of section 2.1), the linear electroaeroelastic behavior of the system can be predicted for increasing airflow speeds. The linear flutter speed of the plate, which corresponds to the neutral stability boundary of the linear system, is 45.4 m·s^{-1}. However, modified aeroelastic behavior is expected due to the presence of nonlinearities. In this work, geometric non-linearity (related to large displacements) is taken into account by replacing the linear FE model by the non-linear FE model (von Kármán) of section 2.2, resulting in a non-linear aeroelastic system. The simulations presented in this section consider the non-linear geometric FE model (to model the steel substructure and also the piezoelectric layer) combined to linear and to non-linear piezoelectricity (as discussed in section 2.1). A

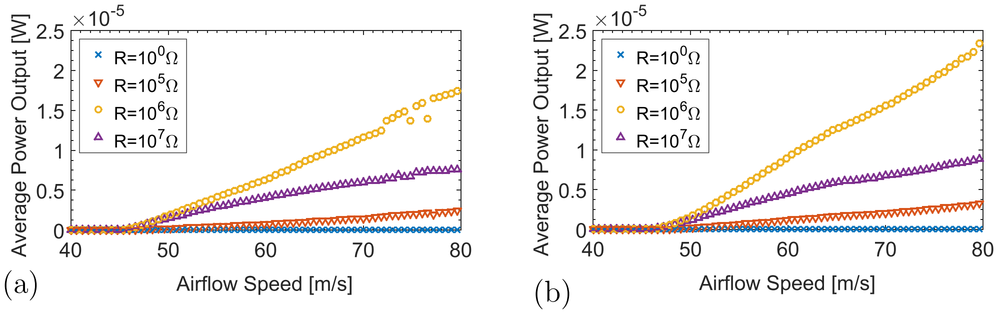

Figure 10. Numerical average power output of the double-bimorph considering (a) linear and (b) non-linear MFC models.

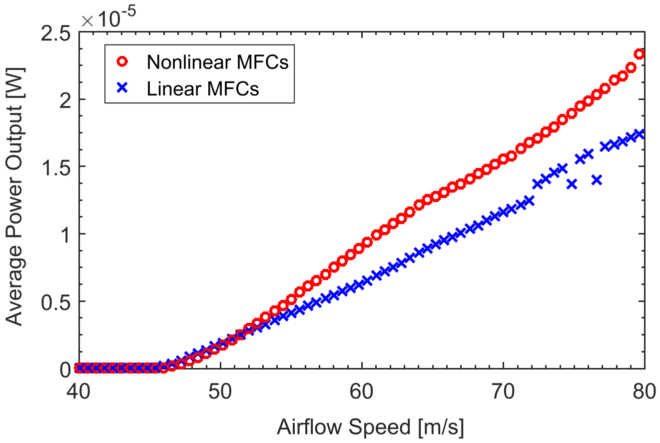

Figure 11. Average power output of the double-bimorph considering the linear and non-linear MFC models for a load resistance of 1 MΩ.

schematic of the double bimorph structure under airflow excitation is presented in figure 7.

The non-linear aeroelastic system considering piezoelectric non-linearity is obtained by combining the non-linear stiffness function (equation (26)) and non-linear electromechanical coupling (equation (27)) in the piezoaeroelastic model (equation (33)). In all simulations (considering linear or non-linear piezoelectricity), different load resistances are assumed individually connected to each MFC to estimate the electrical power output over a range of airflow speeds (40 m·s^{-1} to 80 m·s^{-1}). The considered resistance values are 1 Ω, 100 kΩ, 1 MΩ, and 10 MΩ.

The predicted displacements (at the tip leading edge, point A of figure 3) are shown in figures 8(a) and (b) considering linear and non-linear MFC models, respectively. Both for the linear and non-linear piezoelectricity, the cut-in speed for limit cycle oscillations (LCOs) is 45.4 m·s^{-1} for a load resistance of 1 MΩ. The critical airflow speed for LCOs is slightly modified for each load resistance considered in both cases. The bifurcations for each resistance case are supercritical (Dimitriadis 2017).

Figure 9 displays the tip displacements for the load resistance of 1 MΩ (the load resistance that leads to the largest cut-in speed in figure 8). Linear and non-linear piezoelectric cases are shown for comparison purposes (in both cases the non-linear geometric model is considered). Tip displacements are smaller for the non-linear piezoelectric case than for the linear piezoelectric case for airflow speeds smaller than 57.0 m·s^{-1}. For larger airflow speeds, tip displacements for the non-linear case are larger than that for the linear case. It is important to note that piezoelectric softening comes with non-linear dissipation under larger amplitudes (Leadenham and Erturk 2015), that is not considered in this work. One should also note that the tip displacement in figure 9 is on the order of the plate thickness (that includes the substructure and the MFCs).

Figure 10 shows the power output with increasing airflow speed for each load resistance. The power output strongly depends on the load resistance assumed in the electrical domain, as shown in figures 10(a) for linear MFC model and 10(b) for non-linear MFC model (in both cases the non-linear geometric model is considered). The reported values of power output represent the total power obtained from the summation of all four circuits. In both (linear and non-linear piezoelectricity) cases, the maximum average power output was predicted for the load resistance of 1 MΩ. For the same load resistance of 1 MΩ, figure 11 shows that the average power output is modified due to the presence of piezoelectric non-linearity.

4. Conclusions

Linear and non-linear models were developed based on finite element analysis for electromechanically coupled structures. The linear model was developed considering Kirchhoff plate assumptions and the geometrically non-linear one using von Kármán's approximation. Moreover, linear and non-linear models were also implemented for the piezoelectric effect.

The non-linear geometric model combined to piezoelectric non-linearity was succesfully validated against experimental results from the literature for an MFC bimorph energy harvesting case. The numerical model predicts the softening behavior for increasing base acceleration levels both when tip velocity and power output are considered. The numerical power output slightly overpredicts the experimental one under large excitations since non-linear dissipative effects are not considered in the model. Numerical results for pure bending actuation case of a double bimorph plate were successfully verified against experimental data. Moreover, the double bimorph behavior under pure twist resonant actuation as well as under combined (bending-twist) resonant actuation was discussed. In the first case, the softening behavior at low excitations is due to piezoeletric non-linearity, while the hardening behavior is due to geometric nonlinearities at high actuation levels. The same behavior was observed for the twist mode when the combined actuation was numerically investigated.

The non-linear structural model was combined to an unsteady aerodynamic model to perform non-linear aeroelastic simulations for wind energy harvesting. The nonlinear aeroelastic behavior was discussed when linear and nonlinear piezoelectric models were considered. The presence of piezoelectric non-linearity modifies the power output as compared to the linear piezoelectric case. Nonlinear structural dissipative effects could also be identified and incorporated in the modeling framework. The resulting modeling and analysis framework is applicable to both energy harvesting and actuation applications in the presence of aerodynamic loads.

Acknowledgments

This study was financed in part by the Coordenação de Aperfeiçoamento de Pessoal de Nível Superior - Brasil (CAPES) - Finance Code 001. It is also supported by CNPq (Brazil) [grant number 141452/2014-5] and by the Sao Paulo Research Foundation (FAPESP) [grant numbers 2014/21827-3, 2015/26045-6, 2016/13717-9 and 2017/08467-6].

ORCID iDs

Jose Augusto de Carvalho Dias https://orcid.org/0000-0002-7099-0295
Vagner Candido de Sousa https://orcid.org/0000-0002-3331-4386
Alper Erturk https://orcid.org/0000-0003-0110-5376
Carlos De Marqui Junior https://orcid.org/0000-0003-4058-1885

References

Abdelkefi A and Hajj M R 2013 Performance enhancement of wing-based piezoaeroelastic energy harvesting through freeplay nonlinearity, *Theor. Appl. Mech. Lett.* **3** 41001

Abdelkefi A, Nayfeh A H and Hajj M R 2012a Design of piezoaeroelastic energy harvesters *Nonlinear Dynamics* **68** 519–30.

Abdelkefi A, Nayfeh A H and Hajj M R 2012b Global nonlinear distributed-parameter model of parametrically excited piezoelectric energy harvesters, *Nonlinear Dynamics* **67** 1147–60

Abdelkefi A, Nayfeh A H and Hajj M R 2012c Modeling and analysis of piezoaeroelastic energy harvesters *Nonlinear Dynamics* **67** 925–39

Albano E and Rodden W P 1969 A doublet-lattice method for calculating lift distributions on oscillating surfaces in subsonic flows. *AIAA Journal* **7** 279–85

Aurelle N, Guyomar D, Richard C, Gonnard P and Eyraud L 1996 Nonlinear behavior of an ultrasonic transducer *Ultrasonics* **34** 187–91

Bae J-S and Inman D J 2014a Aeroelastic characteristics of linear and nonlinear piezo-aeroelastic energy harvester *J. Intell. Mater. Syst. Struct.* **25** 401–16

Bae J-S and Inman D J 2014b Aeroelastic characteristics of linear and nonlinear piezo-aeroelastic energy harvester *J. Intell. Mater. Syst. Struct.* **25** 401–16

Bisplinghoff R, Ashley H and Halfman R 1996 *Aeroelasticity* Dover Books on Aeronautical Engineering Series (New York: Dover) (https://books.google.com.br/books?id=jtqDQ2nTvvcC)

Bruni C, Gibert J, Frulla G, Cestino E and Marzocca P 2017 Energy harvesting from aeroelastic vibrations induced by discrete gust loads *J. Intell. Mater. Syst. Struct.* **28** 47–62

Crisfield M A 1997 *Non-Linear Finite Element Analysis of Solids and Structures: Advanced Topics* 1st edn (New York, NY, USA: Wiley)

De Marqui C, Erturk A and Inman D J 2009 An electromechanical finite element model for piezoelectric energy harvester plates *J. Sound Vib.* **327** 9–25

De Marqui C, Erturk A and Inman D J 2010 Piezoaeroelastic modeling and analysis of a generator wing with continuous and segmented electrodes *J. Intell. Mater. Syst. Struct.* **21** 983–93

De Marqui C, Tan D and Erturk A 2018 On the electrode segmentation for piezoelectric energy harvesting from nonlinear limit cycle oscillations in axial flow *J. Fluids Struct.* **82** 492–504

De Marqui C, Vieira W G R, Erturk A and Inman D J 2011 Modeling and analysis of piezoelectric energy harvesting from aeroelastic vibrations using the Doublet-Lattice method *J. Vib. Acoust.* **133** 011003

De Sousa V C and De Marqui Junior C 2015 Airfoil-based piezoelectric energy harvesting by exploiting the pseudoelastic hysteresis of shape memory alloy springs, *Smart Mater. Struct.* **24** 125014

Deraemaeker A, Nasser H, Benjeddou A and Preumont A 2009 Mixing rules for the piezoelectric properties of macro fiber composites *J. Intelligent Mater. Syst. Struct.* **20** 1475–82

Dias J A C, De Marqui C and Erturk A 2013 Hybrid piezoelectric-inductive flow energy harvesting and dimensionless electroaeroelastic analysis for scaling, *Appl. Phys. Lett.* **102** 044101

Dimitriadis G 2017 Aerospace Series *Introduction to Nonlinear Aeroelasticity* (New York: Wiley) (https://books.google.com.br/books?id=pelcvgAACAAJ)

Dowell E H and Tang D 2002 Nonlinear Aeroelasticity and Unsteady Aerodynamics, *AIAA J.* 40 1697–707

Dunnmon J A, Stanton S C, Mann B P and Dowell E H 2011 Power extraction from aeroelastic limit cycle oscillations, *J. Fluids Struct.* **27** 1182–98

Erturk A, Vieira W G R, De Marqui C and Inman D J 2010 On the energy harvesting potential of piezoaeroelastic systems *Appl. Phys. Lett.* **96**

Goldschmidtboeing F, Eichhorn C, Wischke M, Kroener M and Woias P 2011 The influence of ferroelastic hysteresis on mechanically excited PZT cantilever beams *PowerMEMS* pp 114–17

Harder R L and Desmarais R N 1972 Interpolation using surface splines. *Journal of Aircraft* **9** 189–91

Hu Y, Xue H, Yang J and Jiang Q 2006 Nonlinear behavior of a piezoelectric power harvester near resonance *IEEE Trans. Ultrason. Ferroelectr. Freq. Control* **53** 1387–91

IEEE Standard on Piezoelectricity 1988 *ANSI/IEEE Std 176-1987* pp 1–74

Javed U, Dai H and Abdelkefi A 2015 Nonlinear dynamics and comparative analysis of hybrid piezoelectric-inductive energy harvesters subjected to galloping vibrations *Eur. Phys. J. Spec. Top.* 224 2929–48

Leadenham S and Erturk A 2015 Unified nonlinear electroelastic dynamics of a bimorph piezoelectric cantilever for energy harvesting, sensing, and actuation *Nonlinear Dynamics* 79 1727–43

Mahmoodi S N, Jalili N and Daqaq M F 2008 Modeling, nonlinear dynamics, and identification of a piezoelectrically actuated microcantilever sensor *IEEE/ASME Trans. Mechatron.* 13 58–65
Michelin S and Doare D 2013 Energy harvesting efficiency of piezoelectric flags in axial flows *J. Fluid Mech.* 714 489–504
Nayfeh A and Mook D 2008 *Nonlinear Oscillations* (New York: Wiley Classics Library) (https://books.google.com.br/books?id=sj3ebg7jRaoC)
Roger K L 1977 Airplane Math Modeling Methods for Active Control Design *AGARD-CP-228* pp 4.1–4.11 (https://ci.nii.ac.jp/naid/10003115109/en/)
Samur A 2013 Flexible piezoelectric composites and concepts for bio-inspired dynamic bending-twisting actuation *Thesis*, Georgia Institute of Technology (https://books.google.com.br/books?id=97ApnQAACAAJ)
Shahab S and Erturk A 2017 Coupling of experimentally validated electroelastic dynamics and mixing rules formulation for macro-fiber composite piezoelectric structures *J. Intelligent Mater. Syst. Struct.* **28** 1575–88
Sousa V C, De M Anicézio M, De Marqui C and Erturk A 2011 Enhanced aeroelastic energy harvesting by exploiting combined nonlinearities: Theory and experiment *Smart Mater. Struct.* **20**
Tan D, Yavarow P and Erturk A 2018a Nonlinear elastodynamics of piezoelectric macro-fiber composites with interdigitated electrodes for resonant actuation *Composite Struct.* **187** 137–43
Tan D, Yavarow P and Erturk A 2018b Resonant nonlinearities of piezoelectric macro-fiber composite cantilevers with interdigitated electrodes in energy harvesting *Nonlinear Dynamics* **92** 1935–45
Tang L, Païdoussis M P and Jiang J 2009 Cantilevered flexible plates in axial flow: Energy transfer and the concept of flutter-mill, *J. Sound Vib.* 326 263–76
Theodorsen T 1935 General theory of aerodynamic instability and the mechanism of flutter
von Karman T 1910 *Festigkeitsprobleme im Maschinenbau* [publisher not identified] Leipzig
von Wagner U and Hagedorn P 2002 Piezo–beam systems subjected to weak electric field: experiments and modelling of non-linearities *J. Sound Vib.* **256** 861–72
Wolf K and Gottlieb O 2001 *Nonlinear Dynamics of a Cantilever Beam Actuated by Piezoelectric Layers in Symmetric and Asymmetric Configuration* p 6
Xiang J, Wu Y and Li D 2015 Energy harvesting from the discrete gust response of a piezoaeroelastic wing: Modeling and performance evaluation *J. Sound Vib.* **343** 176–93
Zienkiewicz O C and Taylor R L 2000 The Finite Element Method *Fluid Dynamics* (Portsmouth, NH: Heinemann) (https://books.google.com.br/books?id=wmDQ_3qzvmIC)